

OPTICS

Stable optical lateral forces from inhomogeneities of the spin angular momentum

Yuzhi Shi^{1,2,3,4*}, Tongtong Zhu⁵, Jingquan Liu⁶, Din Ping Tsai^{7*}, Hui Zhang⁸, Shubo Wang⁹, Che Ting Chan¹⁰, Pin Chieh Wu¹¹, Anatoly V. Zayats¹², Franco Nori^{13,14*}, Ai Qun Liu^{8*}

Transverse spin momentum related to the spin angular momentum (SAM) of light has been theoretically studied recently and predicted to generate an intriguing optical lateral force (OLF). Despite extensive studies, there is no direct experimental evidence of a stable OLF resulting from the dominant SAM rather than the ubiquitous spin-orbit interaction in a single light beam. Here, we theoretically unveil the nontrivial physics of SAM-correlated OLF, showing that the SAM is a dominant factor for the OLF on a nonabsorbing particle, while an additional force from the canonical (orbital) momentum is exhibited on an absorbing particle due to the spin-orbit interaction. Experimental results demonstrate the bidirectional movement of 5- μm -diameter particles on both sides of the beam with opposite spin momenta. The amplitude and sign of this force strongly depend on the polarization. Our optofluidic platform advances the exploitation of exotic forces in systems with a dominant SAM, facilitating the exploration of fascinating light-matter interactions.

INTRODUCTION

Light carries momenta that can be transferred to objects and exert optical forces. Since the seminal work by Ashkin *et al.* (1), the optical radiation pressure force (2) and gradient force (1) have enabled numerous physical and biological applications (3–8). Optical “tractor beams” provide an additional degree of freedom to optical micro-manipulation by exploiting the dominant forward scattering (9–13). The optical lateral force (OLF), which represents a particular category of force perpendicular to the wave vector (14–16), has attracted a great deal of interest due to its intriguing physics and potential applications in enantiomer sorting (17–19). By virtue of the spin-orbit coupling from the circularly polarized beam (20–22), the OLF can be generated on an achiral particle placed above or at the surface, which breaks the mirror symmetry of the light scattering (14, 15, 23, 24). Linearly polarized beams have also been able to exert reversible OLFs on chiral microparticles by lateral momenta transfer (17) or plasmonic directional side scattering (25). Aside from using interfaces, OLFs can emerge on chiral particles in complex optical fields, for instance, wave interference (26–28) and evanescent waves (18). Despite these extensive explorations, few attempts have been devoted

to achieving an OLF on an achiral particle using a simple light beam in a homogeneous environment.

An elliptically polarized beam, when tightly focused, transfers the spin momentum into the canonical (or orbital) momentum by the spin-orbit interaction to move the metallic particle in a circular orbit (29–32). Recently, the extraordinary transverse spin (33–41), which is orthogonal to the wave vector, has been theoretically investigated in such highly focused optical field. Although the nonequilibrium and unstable transverse force from the transverse spin might have been observable in a focused circularly polarized beam, the dominant optical gradient force could attract the particle to a stable trapping position where no transverse force exists. Meanwhile, this transient transverse force can also be overwhelmed by thermal fluctuations or the spin-orbit interaction (36). Thus, it cannot be truly considered a stable OLF. Besides, the recently reported orbiting of a particle in a focused ring-shaped field with a radial intensity gradient was unambiguously attributed to the spin-to-orbit conversion (31), whereas the comprehensive analysis of the transverse force from a system with dominant spin angular momenta (SAMs) still remains elusive as highly focused beams induce predominant spin-orbit interactions (29). In addition to highly focused beams, the transverse spin and force have been theoretically discovered in evanescent waves (15, 32) and structured beams (35). The measurements of the transverse spin and force were reported with scanning a particle through the focal plane of the beam (42, 43), using a nanocantilever (44), or a three-dimensional force spectroscopy (45). Transverse spin was experimentally demonstrated in structured electromagnetic guided waves, such as surface Bessel beams and Airy beams (46). The spin was also found in the unpolarized paraxial light (47), in the evanescent waves (48), in surface acoustic waves (49), and using an atomic force microscope tip for the quantum sensing of photonic spin density (50). A summary of the transverse spin and potential force effects can be found in table S1. Despite ubiquitous efforts, to the best of our knowledge, there is no direct demonstration of the spin momentum–induced stable OLF in a single optical beam without the contribution of the prevalent spin-orbit interaction.

¹Institute of Precision Optical Engineering, School of Physics Science and Engineering, Tongji University, Shanghai 200092, China. ²MOE Key Laboratory of Advanced Micro-Structured Materials, Shanghai 200092, China. ³Shanghai Institute of Intelligent Science and Technology, Tongji University, Shanghai 200092, China. ⁴Shanghai Frontiers Science Center of Digital Optics, Shanghai 200092, China. ⁵School of Optoelectronic Engineering and Instrumentation Science, Dalian University of Technology, Dalian 116024, China. ⁶National Key Laboratory of Science and Technology on Micro/Nano Fabrication, Shanghai Jiao Tong University, Shanghai 200240, China. ⁷Department of Electrical Engineering, City University of Hong Kong, Hong Kong, China. ⁸School of Electrical and Electronic Engineering, Nanyang Technological University, Singapore 639798, Singapore. ⁹Department of Physics, City University of Hong Kong, Hong Kong, China. ¹⁰Department of Physics, The Hong Kong University of Science and Technology, Hong Kong, China. ¹¹Department of Photonics, National Cheng Kung University, Tainan 70101, Taiwan. ¹²Department of Physics and London Centre for Nanotechnology, King's College London, London, UK. ¹³Theoretical Quantum Physics Laboratory, RIKEN Cluster for Pioneering Research, Wakoshi, Saitama 351-0198, Japan. ¹⁴Physics Department, University of Michigan, Ann Arbor, MI 48109-1040, USA.

*Corresponding author. Email: yuzhi_shi01@163.com (Y.S.); dptsai@cityu.edu.hk (D.P.T.); fnori@riken.jp (F.N.); eaqliu@ntu.edu.sg (A.Q.L.)

Here, we demonstrate that a stable spin-correlated OLF on a nonabsorbing sphere is possible to achieve even when using a single beam in a homogeneous environment. The beam is loosely focused into a line-shaped spot with widths much larger than the wavelength, thus significantly diminishing the force from the spin-orbit interaction. The OLF from the inhomogeneity of the SAM can appear in the loosely focused beam. The particle is immersed in a liquid medium with the same refractive indices as top and bottom quartz slides, mimicking a perfect homogeneous environment. Theoretical investigations reveal that the spin momentum (proportional to the curl of the SAM, \mathbf{S}) dominantly contributes to the OLF on a nonabsorbing nanoparticle. Experimental results demonstrate that 5- μm -diameter particles move bidirectionally on both sides of the beam with opposite spin momenta. The amplitude and direction of the OLF can be robustly controlled by different helicities of light. Our optofluidic

strategy provides a novel opportunity to harness exotic optical forces on various kinds of particles (e.g., high index, metal, and chiral) from the optical spin and other intrinsic properties of light.

RESULTS

Principle and theoretical modeling of the spin-angular-momentum-dependent optical lateral force

To investigate the intriguing OLF in a single beam in a homogeneous environment, a laser beam (wavelength $\lambda = 532 \text{ nm}$) is focused into a line-shaped optical field as illustrated in Fig. 1A, whose widths in two orthogonal directions are controlled by two cylindrical lenses (fig. S1). The particle is immersed in a liquid medium, which is sandwiched by two glass slides. To ensure a homogeneous environment and eliminate the interference from the reflected light, the liquid polyethylene

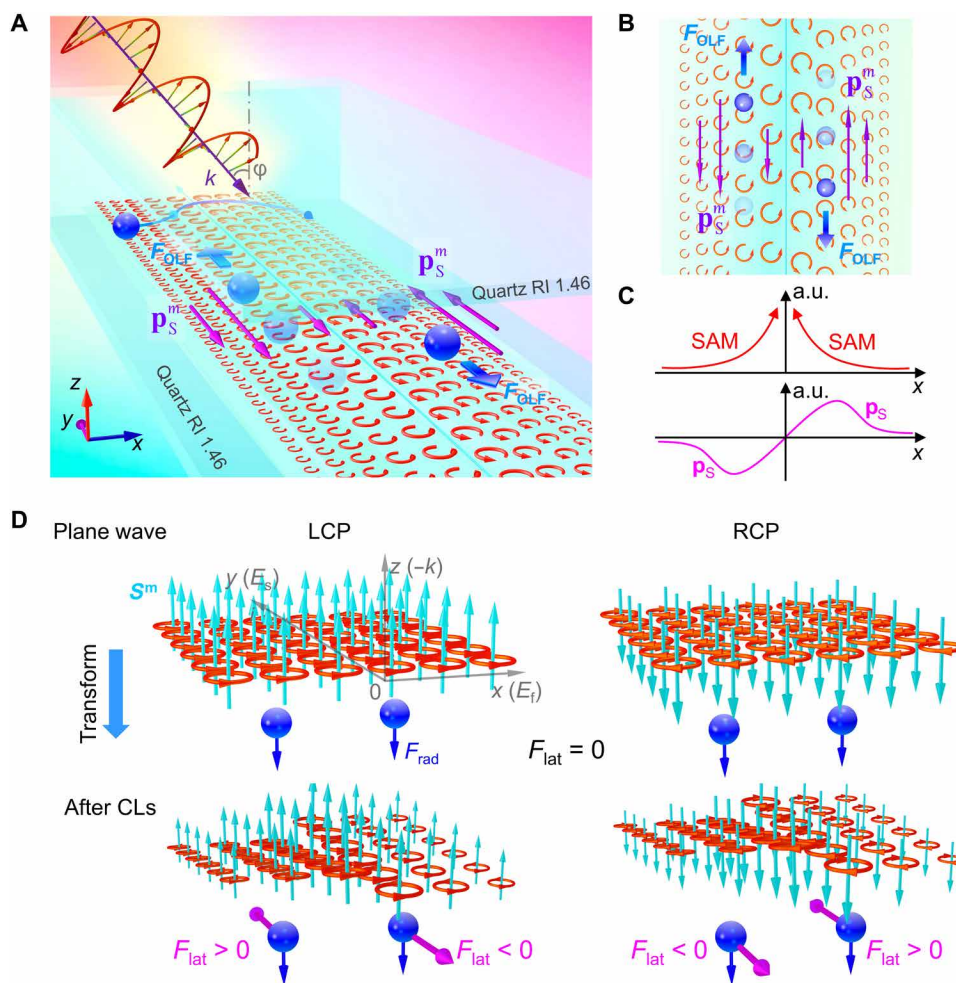


Fig. 1. Origin of the spin-correlated optical lateral force in a single line-shaped beam. (A) Illumination geometry for a particle immersed inside a medium sandwiched by two quartz slides. The medium and two quartz slides have the same refractive index of 1.46. A circularly polarized incident beam is focused into a line shape and is obliquely incident onto the particle at an angle φ . Seeing toward the $-z$ direction, when the beam has a left-handed circular polarization (LCP), the particles on the left and right sides of the beam move along the $+y$ and $-y$ directions, respectively, and along the opposite directions of the magnetic spin momentum density \mathbf{p}_S^m , as also sketched in (B). (C) The inhomogeneity of the SAM in the x direction induces the spin momentum density \mathbf{p}_S in the y direction and consequently generates the OLF on a nonabsorbing particle along the opposite direction of \mathbf{p}_S , a.u., arbitrary units. (D) Helicity-dependent magnetic SAM \mathbf{S}^m and optical force before and after focusing by two cylindrical lenses (CLs). The distribution of \mathbf{S}^m is homogeneous for a plane wave. \mathbf{S}^m points to the $+z$ direction when the angle θ of the quarter-wave plate is 45° (LCP). The corresponding OLFs after focusing by CLs point along the $+y$ and $-y$ directions at $x < 0$ and $x > 0$, respectively. In contrast, \mathbf{S}^m points to the $-z$ direction when $\theta = 135^\circ$ [right-handed circular polarization (RCP)]. The corresponding OLFs point along the $-y$ and $+y$ directions at $x < 0$ and $x > 0$, respectively. \mathbf{S}^m equals zero when $\theta = n \times 90^\circ$ ($n = 0, 1, 2, \dots$).

glycol is delicately chosen to have the same refractive index as the glass (quartz, refractive index equals 1.46) (Fig. 1A). Because of the line-shaped light field, the SAM, \mathbf{S} , visualized by the loops in Fig. 1A, is nonuniformly distributed in the x direction and decays from the center of the beam ($x = 0$). All loops rotate anticlockwise (top view), indicating that the sign of \mathbf{S} only depends on the helicity of the beam and does not change through the whole field. Meanwhile, the different decaying directions of \mathbf{S} in the x direction result in opposite spin momentum densities \mathbf{p}_S , which can be expressed as (32, 51)

$$\begin{aligned} \mathbf{p}_S &= \mathbf{p}_S^e + \mathbf{p}_S^m = \frac{1}{2} \nabla \times \mathbf{S} \\ &= \frac{g}{4\omega} \text{Im} \left[\nabla \times \left(\frac{1}{\mu} \mathbf{E}^* \times \mathbf{E} \right) + \nabla \times \left(\frac{1}{\epsilon} \mathbf{H}^* \times \mathbf{H} \right) \right] \end{aligned} \quad (1)$$

where \mathbf{p}_S^e and \mathbf{p}_S^m are spin momenta from electric and magnetic field contributions, $g = (8\pi)^{-1}$ in Gaussian units, and ϵ and μ are the permittivity and permeability of the medium, respectively. To investigate the \mathbf{p}_S -dependent OLF, the electric field of the focused in-paraxial wave beam can be approximately written as

$$\mathbf{E} = A(\cos \theta \bar{\mathbf{x}} + i \sin \theta \bar{\mathbf{y}}) \exp \left[-\left(\frac{x^2}{w_x^2} + \frac{y^2}{w_y^2} \right) \right] \exp(-ikz) \quad (2)$$

where A is the wave amplitude, $\bar{\mathbf{x}}$ and $\bar{\mathbf{y}}$ are unit vectors of the corresponding axes, and k is the wave number in the medium; θ is the angle between the electric field of the light beam and the fast axis of the quarter-wave plate (also the x axis); w_x and w_y are the half focal widths in the x and y directions, respectively (fig. S1). In the experiment, w_x and w_y are 15 and 500 μm , respectively, which are much larger than λ (532 nm), so we can ignore the beam divergence and largely reduce the effect of the spin-orbit interaction. The explicit expression (52) of the optical force can be written as $\mathbf{F} = \mathbf{F}_e + \mathbf{F}_m + \mathbf{F}_{em}$, where \mathbf{F}_e , \mathbf{F}_m , and \mathbf{F}_{em} express the electric dipole force, magnetic dipole force, and force from the interference between the electric and magnetic dipoles, respectively. \mathbf{F}_e or \mathbf{F}_m emerges from the contributions of the electric or magnetic part of the inhomogeneous energy distribution (gradient force) and the orbital momentum density (see eqs. S12 and S16). After an explicit derivation (notes S1 and S2), $\mathbf{F}_e = 0$ because of the vanished gradient force and electric orbital momentum when the particle is placed at $y = 0$ (see eq. S15). Thus, the OLF becomes

$$\begin{aligned} \mathbf{F}_{\text{OLF}}(x, 0) &= \mathbf{F}_m + \mathbf{F}_{em} \\ &= \frac{\omega}{g} \left[\epsilon \text{Im}(\alpha_m) \mathbf{p}_O^m - \frac{k^3}{3} \text{Re}(\alpha_e \alpha_m^*) (\mathbf{p}_S^m + \mathbf{p}_O^m) \right] \\ &= \frac{2A^2 c^2 \sin \theta \cos \theta x}{\omega^2 \mu^2 w_x^2 w_y^2} \left[\text{Im}(\alpha_m) - \frac{k^3 w_y^2}{3\epsilon} \text{Re}(\alpha_e \alpha_m^*) \left(k^2 + \frac{1}{w_y^2} \right) \right] \exp \left(-\frac{2x^2}{w_x^2} \right) \bar{\mathbf{y}} \end{aligned} \quad (3)$$

where α_e and α_m are the complex electric and magnetic polarizabilities, \mathbf{p}_O^m is the magnetic orbital momentum density, c is the speed of light in vacuum, and ω is the angular frequency of light. For a nonabsorbing particle, $\text{Im}(\alpha_m) = 0$, resulting in $\mathbf{F}_{\text{OLF}} = \mathbf{F}_{em}$, the force is only related to $\text{Re}(\alpha_e \alpha_m^*) (\mathbf{p}_S^m + \mathbf{p}_O^m)$ ($\mathbf{p}_S^e = 0$ according to eq. S33). Intriguingly, for different orientation angles θ of the quarter-wave plate, the sign of the OLF oscillates with a period of π (Eq. 3; see also fig. S2). Thus, from Eq. 1, by plotting the distributions of magnetic SAM S^m and the magnetic spin momentum \mathbf{p}_S^m (\mathbf{p}_O^m is

negligible when $w_y \gg \lambda$; see discussions below), we can infer opposite directions of the OLF on the two sides of the beam center ($x = 0$) in Fig. 1 (A and B). According to Eqs. 1 and 2

$$\begin{aligned} S^m &= \frac{gA^2 c^2 k}{\epsilon \mu^2 \omega^3} \exp \left[-2 \left(\frac{x^2}{w_x^2} + \frac{y^2}{w_y^2} \right) \right] \\ &\left(\frac{2 \cos^2 \theta y}{w_y^2} \bar{\mathbf{x}} - \frac{2 \sin^2 \theta x}{w_x^2} \bar{\mathbf{y}} + k \sin \theta \cos \theta \mathbf{z} \right) \end{aligned} \quad (4)$$

where \mathbf{z} is the unit vector of the z axis.

Note that the spin-to-orbital angular momentum conversion has been widely found in highly focused beams and interpreted using the helicity-dependent geometric phase (29, 31, 53–55). This conversion induces an orbital momentum \mathbf{p}_O and consequently the rotation optical force to move particles in a circular orbit (eqs. S12, S16, and S18). However, in the loosely focused beam described by Eq. 2, the contribution of the orbital momentum can be hugely diminished according to Eq. 3, which shows that the magnetic dipole force term related to \mathbf{p}_O^m is zero because $\text{Im}(\alpha_m) = 0$ for a nonabsorbing particle. Only the force from the interference between the electric and magnetic dipoles contributes to the OLF. In this case, the OLF has contributions from both \mathbf{p}_S^m and \mathbf{p}_O^m , with a ratio of $k^2/(w_y^2)^{-1}$ (see Eq. 3), which can be $\gg 1$ when $w_y \gg \lambda$, meaning that the force from the spin momentum is much larger than that from the orbital momentum. Therefore, we can conclude that the OLF comes predominantly from the inhomogeneity of the SAM or the spin momentum rather than spin-orbit interactions in this loosely focused beam with $w_y \gg \lambda$. The force from the orbital momentum can be prominent when $w_y \sim \lambda$ in a highly focused beam or when the particle has absorption [i.e., $\text{Im}(\alpha_m) \neq 0$ for a metallic particle; see eq. S30].

The intensity gradient of the beam in the x direction gives rise to an inhomogeneous distribution of the SAM, as shown in Fig. 1B. The SAM \mathbf{S} decays from the center of the beam along the $-x$ and $+x$ directions, which also generates opposite distributions of the spin momentum \mathbf{p}_S on both sides of the beam axis, as shown in Fig. 1C. Consequently, the OLF emerges from the spin momentum according to Eq. 3. Thus, the general origin of this SAM-dependent optical force, not just limited to the OLF here, is as follows: Any helicity beam with the SAM gives rise to a SAM inhomogeneity-dependent optical force when the beam has an electric or magnetic gradient that induces a spin momentum \mathbf{p}_S (Eq. 1). This particular force is parallel to the spin momentum vector, which consists of both the electric (\mathbf{p}_S^e) and magnetic (\mathbf{p}_S^m) contributions. The OLF can be in the same or opposite direction of \mathbf{p}_S , depending on the sign of $\text{Re}(\alpha_e \alpha_m^*)$ (see Eq. 5). In most typical scenarios, the SAM inhomogeneity-dependent force only considers the electric spin momentum \mathbf{p}_S^e on an electric dipole (56, 57), which is usually very weak and can be easily overwhelmed by the optical force from the rotating Poynting vectors or the orbital momentum in vortex beams (58, 59), the spin-orbit interaction-induced orbital momentum in highly focused beams (29, 33), and the most common optical gradient forces in various interference fields (35, 60). The magnetic spin momentum \mathbf{p}_S^m plays a crucial role in the spin-dependent magnetic dipole force and the force from the interference between the electric and magnetic dipoles, which is commonly neglected. Despite the rarely unveiled and complex nature of this SAM inhomogeneity-dependent force, it

has already ubiquitously existed in various configurations, which we summarize in table S1.

Before being focused by two cylindrical lenses, a plane wave after the quarter-wave plate always has a homogeneous \mathbf{S}^m , regardless of the different orientation angles θ (Fig. 1B). The OLF does not occur even for different amplitudes of \mathbf{S}^m , under, for instance, $\theta = \pi/8$ (fig. S5) and $\theta = \pi/4$ [left-handed circular polarization (LCP)], as well as different signs of \mathbf{S}^m under $\theta = \pi/4$ and $\theta = 3\pi/4$ [right-handed circular polarization (RCP)]. In this case of a plane wave, only the radiation pressure force works on the particle because $\mathbf{p}_S = \frac{1}{2}\nabla \times \mathbf{S} = 0$ (32, 35), which induces a zero OLF, as indicated in Eq. 3. After focusing (bottom row of Fig. 1D), the inhomogeneity of \mathbf{S}^m (Eq. 4) induces a negative OLF for $\theta = \pi/4$, and a positive OLF for $\theta = 3\pi/4$, on the particle placed at $x > 0$. Meanwhile, opposite OLFs occur for the same θ when the particle is placed at $x < 0$. As shown in Eq. 4 and Fig. 1D, \mathbf{S}^m has components in the x , y , and z directions after focusing, indicating that, in general, the spin-correlated force has three components. This force in the x direction depends on the inhomogeneity of the SAM in the y direction and can be neglected for left and right circularly polarized beams when $w_y \gg w_x$. This is because the OLF is in the same or the opposite direction of the spin momentum \mathbf{p}_S (Eq. 3), which is proportional to the curl of the SAM, i.e., $\mathbf{p}_S = \frac{1}{2}\nabla \times \mathbf{S}$. Therefore, the larger curl of the field gives rise to a larger spin-dependent force. The spin-dependent force in the x direction when the particle is placed at $x = 0$ can be easily obtained from Eq. 3, as shown in eq. S40, showing that the spin-dependent force in the x direction is much smaller than that in the y direction because $\mathbf{p}_S^y \gg \mathbf{p}_S^x$ caused by $w_y \gg w_x$. The optical radiation pressure force toward the $-z$ direction is balanced by the supporting force from the substrate because the particle resides on the surface of the substrate. Consequently, we only need to consider the y -component force (OLF) induced by the inhomogeneity of the SAM, manifesting this configuration as a paradigm for probing the spin-dependent optical force.

Simulation of the optical lateral force

The mathematical derivation of the OLF (Eq. 3) is only applicable to the dipole particle with a radius $a \ll \lambda$. To assess the magnitude of the OLF for larger particles beyond the dipole limit, for instance, $a \sim \lambda$, we performed systematic numerical simulations using the Minkowski stress tensor (see Materials and Methods for simulation details) in the commercial finite element software COMSOL. To eliminate the influence of the optical gradient force in the y direction, we placed the particles at the symmetric axis $y = 0$ and moved them from the region “ $x < 0$ ” to “ $x > 0$.” We simulate the OLF, F_y , and the force in the x direction, F_x (composed of the optical gradient force and the spin-correlated force in the x direction), with different w_y to investigate the effect of the beam expansion in the y direction (Fig. 2A). The amplitude of F_y rises when w_y is increased from 1 to 5 μm and stops rising when w_y is further increased to infinity. $w_y \rightarrow \infty$ results in $\frac{y^2}{w_y^2} \rightarrow 0$ in Eq. 2, meaning that the beam does not diverge in the y direction. The beam becomes a pure plane wave when $w_x = w_y \rightarrow \infty$. The sign of the OLF turns from negative to positive when the particle moves from the region $x < 0$ to $x > 0$, coinciding with the right-handed beam, while F_x attracts the particle to the central point ($x = 0$). The maximum F_x for $w_x = 500 \mu\text{m}$ is almost 50 times larger than the maximum OLF, but this ratio can be significantly reduced when the beam is expanded in the x direction (e.g., $w_y = 15 \mu\text{m}$).

We then consider a practical case with the parameters used in the experiment, e.g., $w_x = 15 \mu\text{m}$ and $w_y = 500 \mu\text{m}$. As shown in Fig. 2B, the OLF is much smaller than that in Fig. 2A because of the decreased field gradient, even if the maximum amplitudes of intensity (at $x = 0$ and $y = 0$; see fig. S1) are the same. The left-handed ($\theta = \pi/4$) and right-handed ($\theta = 3\pi/4$) circular polarizations induce the opposite forces with the same amplitude, indicating the spin-correlated characteristics (force from the curl of \mathbf{S}^m). The sign of the OLF on a nonabsorbing particle (refractive index equals 1.56) reverses from positive to negative for $\theta = \pi/4$ when crossing from the region $x < 0$ to $x > 0$, in agreement with Eq. 3 and the plot of \mathbf{p}_S^m in Fig. 1B. Because w_x and w_y are 15 and 500 μm in the experiment, respectively, the gradient force in the y direction is expected to be tens of times weaker than that in the x direction. The effect from the gradient force in the y direction can be further mitigated when the particle size is at the microscale, which can be approximately predicted from the dipole model: The optical gradient force and spin-correlated OLF are proportional to a^3 and a^8 (a is the particle radius), respectively. Thus, increasing the particle radius will markedly increase the ratio of the OLF and the gradient force. Meanwhile, the increased size significantly increases the magnitude of OLF on the particle (Fig. 2C), thus reducing the influence of the Brownian motion, facilitating the observation of the OLF (61). The maximum radius used for the simulation of the OLF is 500 nm because the OLF is very sensitive to the mesh used in the simulation (see Materials and Methods for simulation details). The OLF can be continuously tuned with the orientation angles of the quarter-wave plate when the particles are placed at $x = 400 \text{ nm}$, as shown in Fig. 2D. When $\theta = 0$ and $\pi/2$, the beams are linearly polarized and the corresponding OLFs are both zero. The OLFs have maximum amplitudes but opposite signs for two circularly polarized beams ($\theta = \pi/4$ and $3\pi/4$). Recently, Ginis *et al.* (62) found that the maxima and minima of the OLF may not necessarily be accompanied by circularly polarized beams. We should also expect this effect to potentially occur in our configuration. We fix the ellipticity angle on the Poincaré sphere to $\pi/2$ (quarter-wave plate) and only consider the orientation angle θ in this work; thus, the maximum OLF here corresponds to a circularly polarized beam. In sharp contrast to the OLF, F_x remains negative with all orientation angles when the particle is at $x > 0$ (see fig. S6). Notably, the OLFs on particles larger than the dipole ($a \sim \lambda$) are calculated rigorously using the Minkowski stress tensor in COMSOL, which increase steadily when increasing the particle size rather than exponentially as indicated by $\text{Re}(\alpha_e \alpha_m^*)$ in the dipole model (Eq. 3), which can be expressed as (32, 63)

$$\text{Re}(\alpha_e \alpha_m^*) \cong \frac{k^2 a^8}{30} \left| \frac{\epsilon_p - \epsilon}{\epsilon_p + 2\epsilon} \right|^2 [\text{Re}(\epsilon_p) + 2] \quad (5)$$

where ϵ_p and μ_p are the permittivity and permeability of the particle, respectively. As seen from Eq. 5, $\text{Re}(\alpha_e \alpha_m^*) > 0$ for a nonabsorbing particle. $\text{Re}(\alpha_e \alpha_m^*)$ can be < 0 for a metallic particle, such as the gold particle, whose $\text{Re}(\epsilon_p) < -2$. Consequently, the OLFs on a nonabsorbing particle and a gold nanoparticle are in the opposite and the same direction of \mathbf{p}_S^m , respectively, as indicated by Eqs. 3 and 5.

Experimental demonstration of optical lateral forces

To facilitate the observation of OLF, we illuminate the particle in a homogeneous environment (see Figs. 1A and 3) with a line-shaped ($w_x = 15 \mu\text{m}$ and $w_y = 500 \mu\text{m}$) obliquely incident beam at an incident angle of 20° . The beam coming from the laser (532 nm,

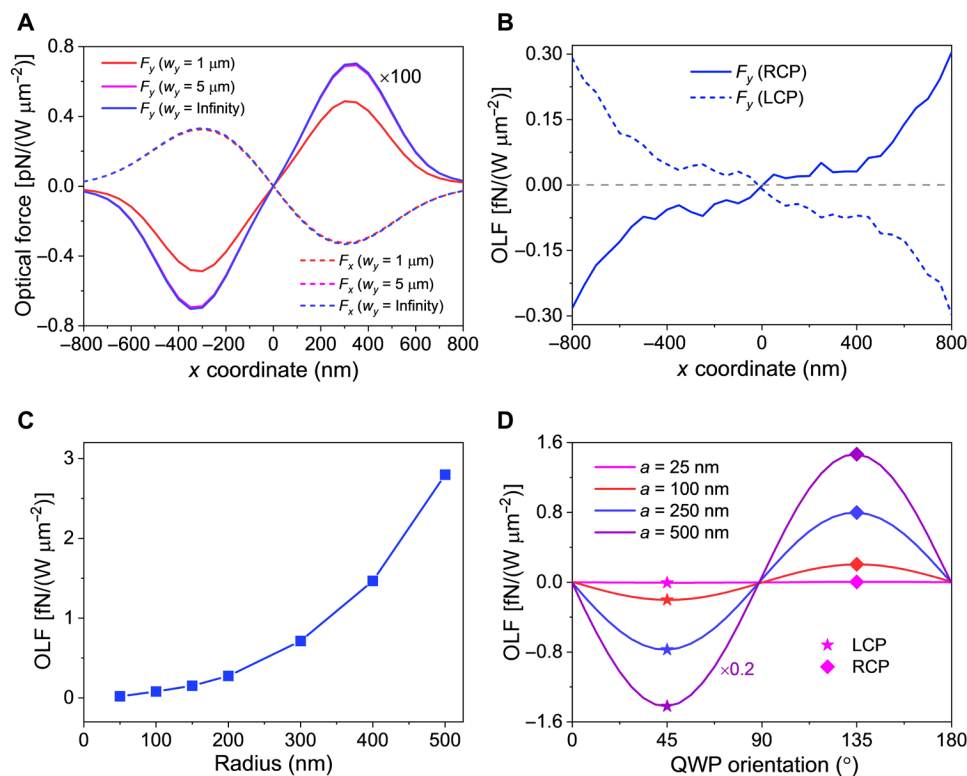


Fig. 2. Numerical calculations of optical forces in the line-shaped beams. (A) Optical forces on a particle in the x direction, F_x , and y direction, F_y , along the x axis for different beam widths w_y . F_x seems to be independent of w_y , while F_y increases with w_y ; the dashed and solid curves represent F_x and F_y , respectively. $a = 50$ nm, $\theta = 3\pi/4$ (RCP, spin σ^+); w_x is set to 500 nm to save the computational memory, and to reveal the pattern of forces when the field gradually decays. (B) OLFs on a particle ($a = 100$ nm) along the x axis under the illuminations of LCP and RCP beams. (C) OLFs on particles with different radii, which are placed at $x = 400$ nm, for the RCP illumination. A maximum radius of 500 nm is simulated (see Materials and Methods for simulation details). (D) Dependence of the OLF with the polarization of the illuminating light for particles with different sizes: The OLF has different signs for LCP and RCP illuminations. S^m equals zero when $\theta = n \times 90^\circ$ ($n = 0, 1, 2, \dots$). Particles are placed at $x = 700$ nm. $w_x = 15$ μm and $w_y = 500$ μm for (B) to (D). Common parameters for (A) to (D) are $\epsilon = (1.46)^2$, $\epsilon_p = (1.56)^2$, and $\mu = \mu_p = 1$. The forces in (A) to (D) are calculated by normalizing the light intensity at ($x = 0, y = 0$) to 1 W/μm².

power of 2 W, Laser Quantum, mpc 6000) initially passes through a 4f system (composed of two lenses with focusing lengths of 15 and 200 mm), so the beam gets expanded for a better focusing quality. Two cylindrical lenses are then used to focus the beam into a line shape. The beam remains perfect inside water, which could be observed using a charge-coupled device (CCD) camera (DS-Ri1, Nikon) to capture the image of diffuse reflection light of a tape sticking on the surface of the bottom quartz plate (17). After dripping a droplet (~10 μl) of polyethylene glycol (refractive index equals 1.46, Sigma-Aldrich) with dispersed 5-μm-diameter polystyrene particles (Polysciences), another quartz plate is placed on top of the droplet to ensure a flat surface and that particles stay in a homogeneous environment. The sandwiched architecture is placed on a hollow stage to prevent the substrate from generating an interfering reflected light beam. Because the particle is not at the interface of air and water, the surface tensor force can be eliminated. The small incident angle is used to generate a small radiation pressure force in the x direction to balance the optical gradient force, which will be discussed in detail in Fig. 4A. Because of the small incident angle, the objective lens should have a relatively long working distance to make sure that it does not block the obliquely incident light. Therefore, a 10× microscope objective [numerical aperture (NA) of 0.3,

Nikon] is used to capture the image of the particle. More information about the setup can be found in Materials and Methods.

Two intriguing scenarios can be observed in the experiment (Fig. 4, A and B). Scenario 1 occurs when the particle is initially located on the left of the beam and near the beam center ($x = 0$), and it experiences an optical radiation pressure force (due to the oblique incidence) and a gradient force both pointing to the $+x$ direction (Fig. 4A). Meanwhile, the OLF deflects the particle in the y direction. The large w_y (500 μm) and 5-μm-diameter particle size used in the experiment ensure that the OLF can dominate the movement of the particle in the y direction by weakening the effect from the optical gradient force. Although the maximum diameter of the particle used in the simulation is 1 μm, which is limited by the large consumed memory of our computer (over 300 Gbytes), the trajectories of particles with different sizes by the OLF follow a similar trend (see Fig. 2). After crossing the $x = 0$ axis, the gradient force in the x direction reverses sign, and the particle eventually stops moving along the x direction (under the balance of the radiation pressure force and the gradient force) and only moves in the y direction, as also shown in figs. S7 and S8. Scenario 2 occurs when the particle is located away from the beam center; the particle now does not experience strong optical radiation pressure or gradient force for a

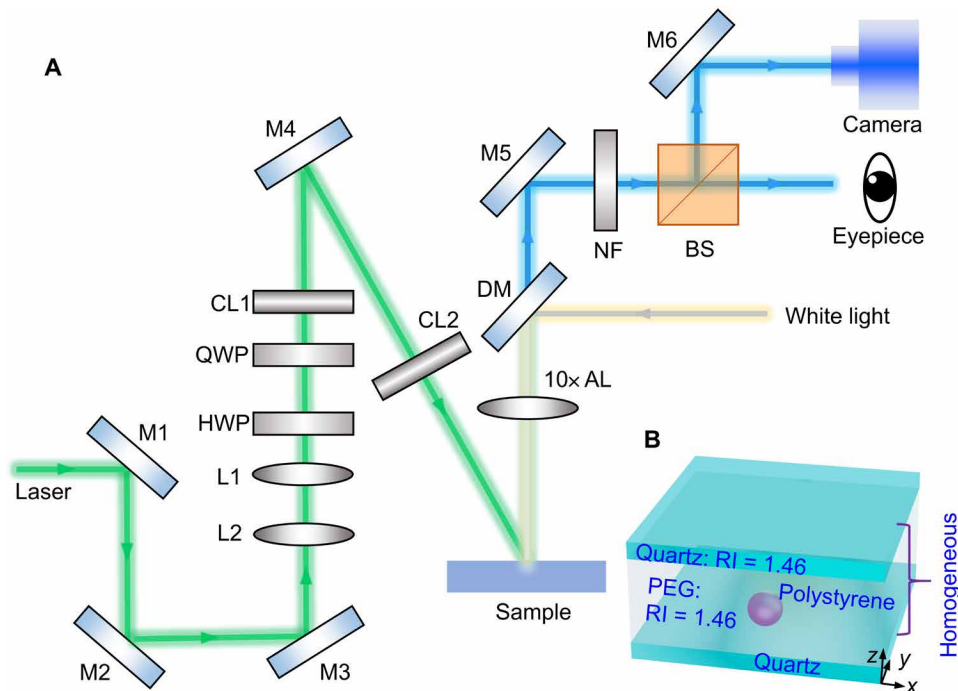


Fig. 3. Experimental configuration. (A) Experimental setup. M, mirror; L1, lens 1 (200 mm); L2, lens 2 (15 mm); HWP, half-wave plate (532 nm); QWP, quarter-wave plate (532 nm); CL1, cylindrical lens 1 (300 mm); CL2, cylindrical lens 2 (75 mm); AL, air lens; DM, dichroic mirror; BS, beam splitter; NF, notch filter (532 nm). (B) Illustration of a particle in a homogeneous environment. Medium: Polyethylene glycol (PEG), refractive index equals 1.46. Up and down quartz glass slides: refractive indices equal 1.46.

motion along in the x direction (Fig. 4B). In this case, as also seen from the experimental results in Fig. 4C, the single 5- μm -diameter particle on the left of the y axis moved along the upright direction under the combined effect of the OLF (upward), optical radiation pressure force, and gradient force (both rightward) when the incident light was LCP (see Fig. 1D). On the contrary, two particles on the right of the y axis moved along the lower-left direction under the combined effect of the OLF (downward), optical radiation pressure force (rightward), and gradient force (leftward).

The experimentally recorded trajectories in the x and y directions in scenario 1, under the illuminations of left-handed and right-handed beams, are shown in Fig. 4 (D and E, respectively). The left-handed (spin σ^-) beam forces the particle to move in the $+y$ and $-y$ directions on the left and right sides of $x = 0$, respectively. The movement trajectory was exactly the opposite for the right-handed (spin σ^+) beam. In contrast, the trajectories in the x direction for both spins followed the same trend of continuously moving particles toward the $+x$ direction until they reach the balance points of optical radiation pressure force and gradient force. The y -direction trajectories of the 5- μm -diameter particles in scenario 2 showed a 0.5- to 1- μm displacement after 150 s (Fig. 4F), corresponding to an OLF of 2.5 to 5 fN, predicted using the equation $F_{\text{OLF}} = F_{\text{drag}} = 6\pi\eta a v$ (64, 65), where F_{drag} is the fluidic drag force, η is the viscosity of the polyethylene glycol medium ($\eta = 0.0161$ Pa·s), and v is the velocity of the particle. The running average of 20 points is used to smooth the raw data to show the moving trend of particles more clearly (66). The viscosity of polyethylene glycol was over 10 times larger than the commonly used water (10^{-3} Pa·s) in optical tweezing experiments, resulting in a moving velocity 10 times slower in the polyethylene glycol than that in water under the same OLF because the drag force

increases linearly with the viscosity. The high viscosity also significantly suppresses the Brownian motion of the particle (5), preventing it from completely overwhelming the OLF and facilitating the observation of the OLF. The Brownian motion is still a non-negligible factor, which induces stochastic signals that greatly influence trajectories of particles as discussed in note S3. For instance, in a short range of time, i.e., a few seconds, the particle may move in the opposite direction of the OLF, as shown in the simulation results of figs. S3 and S4, which is also reflected in the experimental trajectories in Fig. 4 (C to F). Meanwhile, the Brownian motion in a low-viscosity liquid, such as water, may overwhelm the OLF because both of them could move the particle in the same dimension (fig. S4C), causing difficulties in observing the bidirectional movements of particles in the y direction on both sides of the beam. We need polyethylene glycol to match the same refractive index of the quartz substrate to provide a homogeneous environment for the particle. More experimental results about the experimental observations of the OLF can be found in figs. S8 to S12.

The measured maximum OLF on 5- μm -diameter particles located on the right side of the beam axis ($x = 0$) under different laser powers is shown in Fig. 5A. When illuminated with left-handed and right-handed beams, particles experienced optical forces in the $-y$ and $+y$ directions, respectively. The OLF increased linearly with laser power, confirming the proposed experimental strategy. The OLF dropped to near zero when the laser power was decreased to 400 mW, due to the friction between the surface and particle, as well as the inertia of particle in the high-viscosity polyethylene glycol medium. We also varied the quarter-wave plate angle θ to investigate the OLF for different illumination polarizations. The corresponding measured OLF is shown in Fig. 5B, fitted using a sine curve (Eq. 3 and Fig. 2D), showing a relatively good agreement between the theory

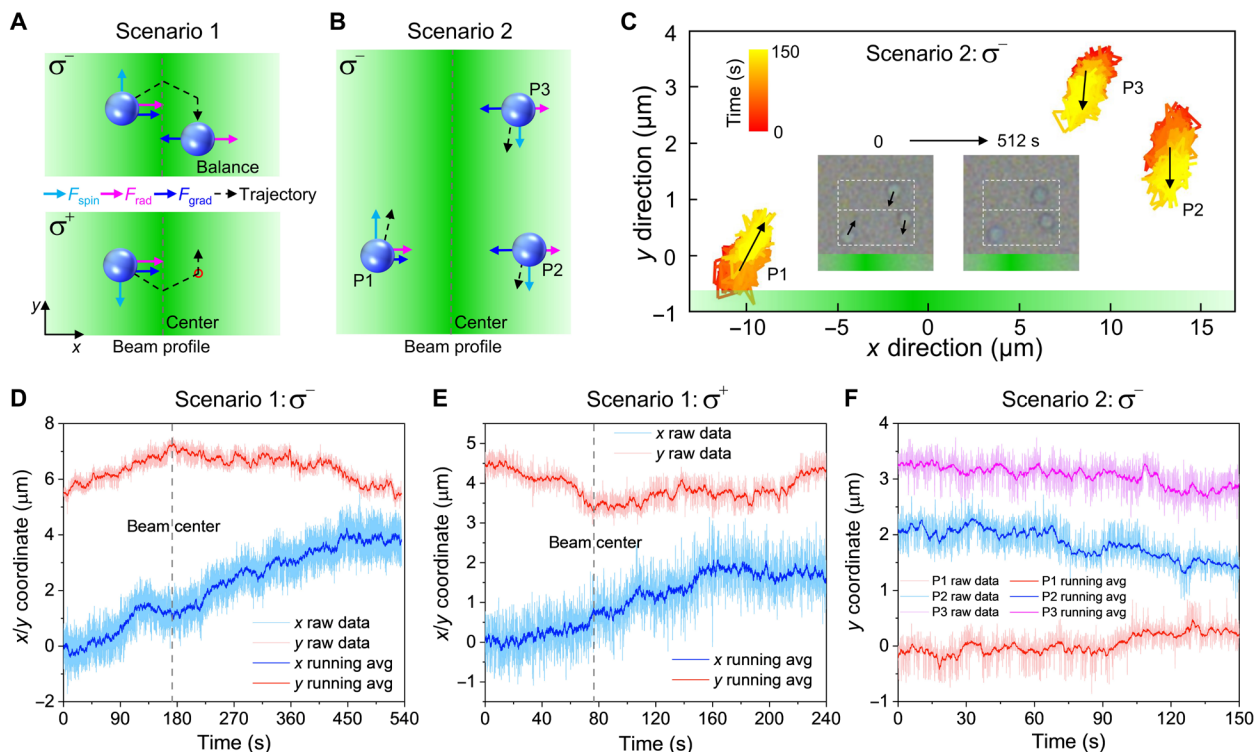


Fig. 4. Experimental observations of optical lateral force induced by the spin angular momentum inhomogeneity. (A) Illustration of scenario 1 where a particle moves in a line-shaped beam: The 5- μm -diameter particle located on the left of the beam and close to the beam center will move across the center due to the optical radiation pressure force, F_{rad} , and gradient force, F_{grad} . The moving trajectories are upward to downward, and downward to upward for LCP and RCP, respectively. (B) Scenario 2: Particles move upward and downward on the left and right sides of the beam, respectively, for an LCP beam. (C) Experimental trajectories of three particles moving in scenario 2 for the LCP beam: P1 moves toward the upright on the left of the beam, while P2 and P3 move downward on the right. (D) Experimental trajectories show that the particle moves from top to bottom in the y direction after crossing the beam center, coinciding with the LCP in scenario 1. The particle moves toward the +x direction until reaching the balance point of F_{rad} and F_{grad} . (E) Experimental trajectories show that the particle moves from bottom to top in the y direction when crossing the beam center, coinciding with the RCP in scenario 1. (F) Experimental trajectories of P1, P2, and P3 in the y direction. The y coordinates of P2 and P3 are down-shifted by 5 and 16 μm for a better comparison. Fitting curves in (D) to (F) are obtained using the running average of 20 points.

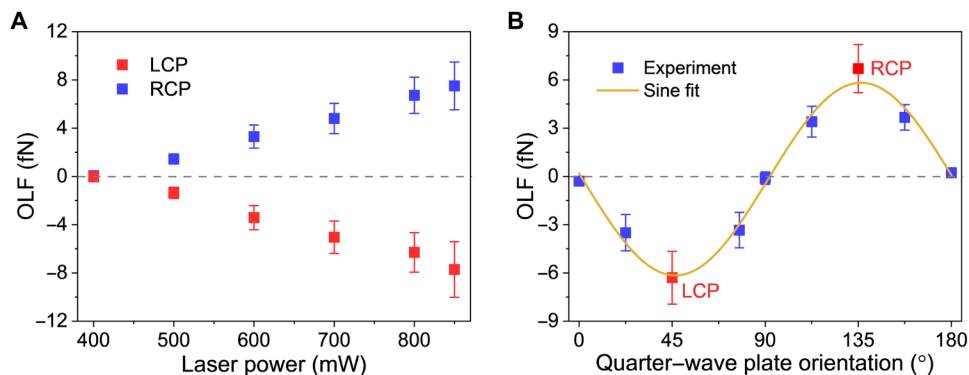


Fig. 5. Quantitative analysis of spin-angular-momentum-correlated optical lateral force. (A) Measured OLFs on 5- μm -diameter particles under different laser powers and polarizations. The OLFs were obtained from the particle velocities using the equation $F_{\text{OLF}} = F_{\text{drag}} = 6\pi\eta a$. (B) Dependence of the measured OLF on 5- μm -diameter particles on the light polarization for a laser power of 800 mW. The squares are the experimental data, and the curve is the sine fit as indicated in Eq. 3. The error bars in (A) and (B) denote the measurement uncertainties.

and experiment. The measured OLF has a period of π and maximum negative and positive values for the left-handed ($\theta = 45^\circ$ or $\pi/4$) and right-handed ($\theta = 135^\circ$ or $3\pi/4$) beams, respectively, showing the exquisite capability to control the movement direction and velocity of the particle transversely, using the spin-correlated OLF in a single laser beam.

DISCUSSION

In addition to intriguing cases demonstrated here, one could also expect other fascinating OLF phenomena in the proposed experimental platform. For instance, instead of negative OLF values for particles residing on the right side of the beam with the LCP, the OLF will be positive when $\text{Re}(\epsilon_p) < -2$ and $\text{Im}(\epsilon_p) \rightarrow 0$ (fig. S13). In the

case of an enhanced positive OLF, the contribution from F_m is negligible compared with F_{em} , showing the important role of the interference between the electric and magnetic dipoles, which is often neglected in the calculation of optical forces. Meanwhile, by exciting multipoles in a high-index nanoparticle (e.g., silicon), one could also expect enhanced spin-correlated OLF (67). Note that the OLF remains negative in the entire parameter space of permittivities of the particle and the surrounding media (fig. S14), even when $\epsilon_p < \epsilon$, which usually changes optical gradient force from attractive to repulsive. This behavior can be seen from Eqs. 3 and 5, which show that the sign of the OLF remains constant when $\text{Im}(\epsilon_p) = 0$ (nonabsorbing particle). Moreover, the developed approach can be applied to investigate the spin-correlated force on special particles (e.g., chiral and composite particles) in a homogeneous environment.

Our approach circumvents the existing restrictions for the generation of stable OLFs, which usually require an interface to break the symmetric light scattering, structured light fields such as interference waves and evanescent waves, or special particles such as chiral particles or helicity-sensitive structures (20). By theoretically investigating the stable OLF in a loosely focused line-shaped beam, the spin momentum was found to be the predominant factor contributing to the force on a symmetric nonabsorbing nanoparticle, while the canonical momentum can also induce a much weaker OLF and exert an extra magnetic force on a metallic nanoparticle. The sign of OLF on nonabsorbing and metallic particles could be opposite, considering their positive and negative real parts of permittivities, respectively (see Eqs. 3 and 5). The 5- μm -diameter microparticle was used in the experiment to enlarge the OLF and mitigate the influence of the Brownian motion. The studied particles were experimentally demonstrated to move bidirectionally on both sides of the beam with velocities and directions strongly dependent on the helicity of light.

Because SAM inhomogeneity-dependent systems exist ubiquitously, such as evanescent waves and standing waves (see table S1 for more configurations), one could expect additional experimental demonstrations of this particular type of force. In general, more attention should be paid to this force when investigating the optical force in a light field with SAM, especially when the field is not tightly focused. In this case, the SAM inhomogeneity-dependent force may compete with the force from the spin-orbit interaction and even the optical gradient force. The remarkable transverse spin shown here provides a degree of freedom to achieve the force from fundamental properties of light and can also find promising applications in controllable directional scattering and efficient spin-direction couplers (29, 38, 41, 48). This study opens up an avenue for using the dominant spin momentum of a simple, loosely focused single light beam for manipulating particles and optical forces, rather than systems with strong spin-orbit interactions. It also sheds light onto the development of nontrivial optofluidic approaches for optical sorting and probing.

MATERIALS AND METHODS

Simulation of the light wave and optical lateral forces

The light wave and rigorous simulation of OLF were performed using a finite element method in COMSOL v.5.4. The large particle size (5 μm) used in the experiment generates a large OLF and reduces the effect of the optical gradient force because the optical gradient

force and spin-correlated OLF are, in the dipole approximation, proportional to a^3 and a^8 , respectively. The large size can also mitigate the effect from the Brownian motion. The 5- μm -diameter particle needs to be placed away from the beam center to investigate OLF along the x direction; thus, the simulation requires a model dimension $>5 \mu\text{m}$, which is far beyond the computational capability of our available workstation with 384 Gbytes of RAM; therefore, the numerical simulations were performed for smaller particles. The SAM or spin-correlated OLF is very sensitive to the mesh and integral boundary surrounding the particle, especially when the particle is close to the beam center. The surrounding integral boundary should be less than 10 nm away from the particle and the maximum mesh should be less than 4 nm to obtain a correct OLF. The mesh of the particle should also be much smaller than the usual simulations. Therefore, we set the gap between the integral boundary and the particle surface to 5 nm. The maximum mesh of the space between them is set to 2 nm, and the maximum meshes of particles are set to 5, 10, 10, 20, and 20 nm for particle radii of 25, 50, 100, 250, and 500 nm, respectively. In addition, the maximum mesh of the medium is set to $0.1\lambda(\epsilon_p)^{-1}$. All these configurations consume over 300 Gbytes of computer memory. The electric field is defined using Eq. 2. The optical forces are calculated by integrating the Maxwell stress tensor in the Minkowski form over the integral surface as

$$\langle F_{\text{OLF}} \rangle = \oint_S \langle \vec{T} \rangle \cdot \hat{n} dA \quad (6)$$

$$\langle T_{ij} \rangle = \frac{1}{2} \left[D_i E_j^* + B_i H_j^* - \frac{1}{2} (\mathbf{D} \cdot \mathbf{E}^* + \mathbf{B} \cdot \mathbf{H}^*) \delta_{ij} \right] \quad (7)$$

Here, the symbol $\langle \cdot \rangle$ means the time average over an oscillation period, \hat{n} is the unit outward normal to the integral surface, and δ_{ij} is the Kronecker delta. The integral of the Minkowski stress tensor is directly coded in COMSOL and evaluated from the field information (Eq. 7) by solving Maxwell equations in COMSOL.

Sample preparation and experimental setup

A suspension of 5- μm -diameter polystyrene particles (Polysciences) was dispersed in polyethylene glycol (Sigma-Aldrich). A single small drop of the solution ($\sim 10 \mu\text{l}$) was gently dripped from a 20- μl syringe (World Precision Instruments) onto the surface of a quartz cover slide. Subsequently, another quartz cover slide was placed on top of the medium to prevent disturbance from the external air currents and ensure a flat surface for the incident light. The refractive index of polyethylene glycol was measured to be 1.46, which was the same as the quartz cover slide. The particle inside polyethylene glycol was then considered to be in a homogeneous environment. The experimental setup (Fig. 3) consisted of external optical components connected to a microscope, which was customized to have three independently mobilized axes. Light from the argon ion laser (532 nm, power of 2 W, Laser Quantum, mpc 6000) was obliquely incident onto the sample at an angle of 20° . The beam was focused into a line-shaped light beam using two cylindrical lenses with focal lengths of 300 and 75 mm. A rotating half-wave plate and a quarter-wave plate were allowed for tuning the polarization of light. Particles were illuminated by a quasi-homogeneous white light source (Nikon) for visualization through a $10\times$ microscope objective (NA of 0.3, Nikon). A 532-nm notch filter (Thorlabs) was used to remove most of the scattered laser light. The movements of particles were recorded by a CCD camera (DS-Ri1, Nikon) with a frame rate of ~ 15 frames per second.

SUPPLEMENTARY MATERIALS

Supplementary material for this article is available at <https://science.org/doi/10.1126/sciadv.abn2291>

REFERENCES AND NOTES

- A. Ashkin, J. M. Dziedzic, J. E. Bjorkholm, S. Chu, Observation of a single-beam gradient force optical trap for dielectric particles. *Opt. Lett.* **11**, 288–290 (1986).
- A. Ashkin, Acceleration and trapping of particles by radiation pressure. *Phys. Rev. Lett.* **24**, 156–159 (1970).
- S. Chu, Nobel Lecture: The manipulation of neutral particles. *Rev. Mod. Phys.* **70**, 685–706 (1998).
- Y. Z. Shi, S. Xiong, Y. Zhang, L. K. Chin, Y. Y. Chen, J. B. Zhang, T. H. Zhang, W. Ser, A. Larsson, S. H. Lim, J. H. Wu, T. N. Chen, Z. C. Yang, Y. L. Hao, B. Liedberg, P. H. Yap, K. Wang, D. P. Tsai, C. W. Qiu, A. Q. Liu, Sculpting nanoparticle dynamics for single-bacteria-level screening and direct binding-efficiency measurement. *Nat. Commun.* **9**, 815 (2018).
- Y. Shi, S. Xiong, L. K. Chin, J. Zhang, W. Ser, J. Wu, T. Chen, Z. Yang, Y. Hao, B. Liedberg, P. H. Yap, D. P. Tsai, C.-W. Qiu, A. Q. Liu, Nanometer-precision linear sorting with synchronized optofluidic dual barriers. *Sci. Adv.* **4**, eaao0773 (2018).
- Y. Shi, H. Zhao, K. T. Nguyen, Y. Zhang, L. K. Chin, T. Zhu, Y. Yu, H. Cai, P. H. Yap, P. Y. Liu, S. Xiong, J. Zhang, C.-W. Qiu, C. T. Chan, A. Q. Liu, Nanophotonic array-induced dynamic behavior for label-free shape-selective bacteria sieving. *ACS Nano* **13**, 12070–12080 (2019).
- D. G. Grier, A revolution in optical manipulation. *Nature* **424**, 810–816 (2003).
- P. Hänggi, P. Talkner, M. Borkovec, Reaction-rate theory: Fifty years after Kramers. *Rev. Mod. Phys.* **62**, 251–341 (1990).
- J. Chen, J. Ng, Z. Lin, C. T. Chan, Optical pulling force. *Nat. Photonics* **5**, 531–534 (2011).
- O. Brzobohatý, V. Karásek, M. Šiler, L. Chvátal, T. Čížmár, P. Zemánek, Experimental demonstration of optical transport, sorting and self-arrangement using a ‘tractor beam’. *Nat. Photonics* **7**, 123–127 (2013).
- H. Li, Y. Cao, L.-M. Zhou, X. Xu, T. Zhu, Y. Shi, C.-W. Qiu, W. Ding, Optical pulling forces and their applications. *Adv. Opt. Photonics* **12**, 288–366 (2020).
- X. Li, J. Chen, Z. Lin, J. Ng, Optical pulling at macroscopic distances. *Sci. Adv.* **5**, eaau7814 (2019).
- A. Novitsky, C.-W. Qiu, H. Wang, Single gradientless light beam drags particles as tractor beams. *Phys. Rev. Lett.* **107**, 203601 (2011).
- S. B. Wang, C. T. Chan, Lateral optical force on chiral particles near a surface. *Nat. Commun.* **5**, 3307 (2014).
- F. J. Rodríguez-Fortuño, N. Engheta, A. Martínez, A. V. Zayats, Lateral forces on circularly polarizable particles near a surface. *Nat. Commun.* **6**, 8799 (2015).
- A. Canaguier-Durang, C. Genet, Plasmonic lateral forces on chiral spheres. *J. Opt.* **18**, 015007 (2015).
- Y. Shi, T. Zhu, T. Zhang, A. Mazzulla, D. P. Tsai, W. Ding, A. Q. Liu, G. Cipparrone, J. J. Sáenz, C.-W. Qiu, Chirality-assisted lateral momentum transfer for bidirectional enantioselective separation. *Light Sci. Appl.* **9**, 62 (2020).
- A. Hayat, J. P. B. Mueller, F. Capasso, Lateral chirality-sorting optical forces. *Proc. Natl. Acad. Sci. U.S.A.* **112**, 13190–13194 (2015).
- N. Kravets, A. Aleksanyan, E. Brasselet, Chiral optical Stern-Gerlach newtonian experiment. *Phys. Rev. Lett.* **122**, 024301 (2019).
- H. Magallanes, E. Brasselet, Macroscopic direct observation of optical spin-dependent lateral forces and left-handed torques. *Nat. Photonics* **12**, 461–464 (2018).
- D. O’Connor, P. Ginzburg, F. J. Rodríguez-Fortuño, G. A. Wurtz, A. V. Zayats, Spin-orbit coupling in surface plasmon scattering by nanostructures. *Nat. Commun.* **5**, 5327 (2014).
- J. Petersen, J. Volz, A. Rauschenbeutel, Chiral nanophotonic waveguide interface based on spin-orbit interaction of light. *Science* **346**, 67–71 (2014).
- S. Sukhov, V. Kajorndejnukul, R. R. Naraghi, A. Dogariu, Dynamic consequences of optical spin-orbit interaction. *Nat. Photonics* **9**, 809–812 (2015).
- T. Zhu, Y. Shi, W. Ding, D. P. Tsai, T. Cao, A. Q. Liu, M. Nieto-Vesperinas, J. J. Sáenz, P. C. Wu, C.-W. Qiu, Extraordinary multipole modes and ultra-enhanced optical lateral force by chirality. *Phys. Rev. Lett.* **125**, 043901 (2020).
- Y. Y. Tanaka, P. Albella, M. Rahmani, V. Giannini, S. A. Maier, T. Shimura, Plasmonic linear nanomotor using lateral optical forces. *Sci. Adv.* **6**, eabc3726 (2020).
- T. Zhang, M. R. C. Mahdy, Y. Liu, J. H. Teng, C. T. Lim, Z. Wang, C.-W. Qiu, All-optical chirality-sensitive sorting via reversible lateral forces in interference fields. *ACS Nano* **11**, 4292–4300 (2017).
- H. Chen, H. Zheng, W. Lu, S. Liu, J. Ng, Z. Lin, Lateral optical force due to the breaking of electric-magnetic symmetry. *Phys. Rev. Lett.* **125**, 073901 (2020).
- H. Chen, C. Liang, S. Liu, Z. Lin, Chirality sorting using two-wave-interference-induced lateral optical force. *Phys. Rev. A* **93**, 053833 (2016).
- K. Y. Bliokh, F. J. Rodríguez-Fortuño, F. Nori, A. V. Zayats, Spin-orbit interactions of light. *Nat. Photonics* **9**, 796–808 (2015).
- Y. Zhao, D. Shapiro, D. McGloin, D. T. Chiu, S. Marchesini, Direct observation of the transfer of orbital angular momentum to metal particles from a focused circularly polarized Gaussian beam. *Opt. Express* **17**, 23316–23322 (2009).
- S.-Y. Huang, G.-L. Zhang, Q. Wang, M. Wang, C. Tu, Y. Li, H.-T. Wang, Spin-to-orbital angular momentum conversion via light intensity gradient. *Optica* **8**, 1231–1236 (2021).
- K. Y. Bliokh, A. Y. Bekshaev, F. Nori, Extraordinary momentum and spin in evanescent waves. *Nat. Commun.* **5**, 3300 (2014).
- K. Y. Bliokh, F. Nori, Transverse and longitudinal angular momenta of light. *Phys. Rep.* **592**, 1–38 (2015).
- M. Neugebauer, T. Bauer, A. Aiello, P. Banzer, Measuring the transverse spin density of light. *Phys. Rev. Lett.* **114**, 063901 (2015).
- A. Y. Bekshaev, K. Y. Bliokh, F. Nori, Transverse spin and momentum in two-wave interference. *Phys. Rev. X* **5**, 011039 (2015).
- V. Svak, O. Brzobohatý, M. Šiler, P. Ják, J. Kaňka, P. Zemánek, S. H. Simpson, Transverse spin forces and non-equilibrium particle dynamics in a circularly polarized vacuum optical trap. *Nat. Commun.* **9**, 5453 (2018).
- Y. Long, J. Ren, H. Chen, Intrinsic spin of elastic waves. *Proc. Natl. Acad. Sci. U.S.A.* **115**, 9951–9955 (2018).
- K. Y. Bliokh, D. Smirnova, F. Nori, Quantum spin Hall effect of light. *Science* **348**, 1448–1451 (2015).
- C. Triolo, A. Cacciola, S. Patané, R. Saija, S. Savasta, F. Nori, Spin-momentum locking in the near field of metal nanoparticles. *ACS Photonics* **4**, 2242–2249 (2017).
- A. Aiello, N. Lindlein, C. Marquardt, G. Leuchs, Transverse angular momentum and geometric spin Hall effect of light. *Phys. Rev. Lett.* **103**, 100401 (2009).
- A. Aiello, P. Banzer, M. Neugebauer, G. Leuchs, From transverse angular momentum to photonic wheels. *Nat. Photonics* **9**, 789–795 (2015).
- P. Banzer, M. Neugebauer, A. Aiello, C. Marquardt, N. Lindlein, T. Bauer, G. Leuchs, The photonic wheel: Demonstration of a state of light with purely transverse angular momentum. *J. Eur. Opt. Soc.* **8**, 13032 (2013).
- M. Neugebauer, J. S. Eismann, T. Bauer, P. Banzer, Magnetic and electric transverse spin density of spatially confined light. *Phys. Rev. X* **8**, 021042 (2018).
- M. Antognozzi, C. R. Bermingham, R. L. Harniman, S. Simpson, J. Senior, R. Hayward, H. Hoerber, M. R. Dennis, A. Y. Bekshaev, K. Y. Bliokh, F. Nori, Direct measurements of the extraordinary optical momentum and transverse spin-dependent force using a nano-cantilever. *Nat. Phys.* **12**, 731–735 (2016).
- L. Liu, A. Di Donato, V. Ginis, S. Kheifets, A. Amirzhan, F. Capasso, Three-dimensional measurement of the helicity-dependent forces on a Mie particle. *Phys. Rev. Lett.* **120**, 223901 (2018).
- P. Shi, L. Du, C. Li, A. V. Zayats, X. Yuan, Transverse spin dynamics in structured electromagnetic guided waves. *Proc. Natl. Acad. Sci. U.S.A.* **118**, e2018816118 (2021).
- J. S. Eismann, L. H. Nicholls, D. J. Roth, M. A. Alonso, P. Banzer, F. J. Rodríguez-Fortuño, A. V. Zayats, F. Nori, K. Y. Bliokh, Transverse spinning of unpolarized light. *Nat. Photonics* **15**, 156–161 (2021).
- F. J. Rodríguez-Fortuño, G. Marino, P. Ginzburg, D. O’Connor, A. Martínez, G. A. Wurtz, A. V. Zayats, Near-field interference for the unidirectional excitation of electromagnetic guided modes. *Science* **340**, 328–330 (2013).
- M. M. Sonner, F. Khosravi, L. Janker, D. Rudolph, G. Koblmüller, Z. Jacob, H. J. Krenner, Ultrafast electron cycloids driven by the transverse spin of a surface acoustic wave. *Sci. Adv.* **7**, eabf7414 (2021).
- F. Kalhor, L.-P. Yang, L. Bauer, Z. Jacob, Quantum sensing of photonic spin density using a single spin qubit. *Phys. Rev. Res.* **3**, 043007 (2021).
- M. V. Berry, Optical currents. *J. Opt. A Pure Appl. Opt.* **11**, 094001 (2009).
- M. Nieto-Vesperinas, J. J. Sáenz, R. Gómez-Medina, L. Chantada, Optical forces on small magnetodielectric particles. *Opt. Express* **18**, 11428–11443 (2010).
- K. Y. Bliokh, E. A. Ostrovskaya, M. A. Alonso, O. G. Rodríguez-Herrera, D. Lara, C. Dainty, Spin-to-orbital angular momentum conversion in focusing, scattering, and imaging systems. *Opt. Express* **19**, 26132–26149 (2011).
- Y. Zhao, J. S. Edgar, G. D. M. Jeffries, D. McGloin, D. T. Chiu, Spin-to-orbital angular momentum conversion in a strongly focused optical beam. *Phys. Rev. Lett.* **99**, 073901 (2007).
- P. B. Monteiro, P. A. M. Neto, H. M. Nussenzveig, Angular momentum of focused beams: Beyond the paraxial approximation. *Phys. Rev. A* **79**, 033830 (2009).
- S. Albaladejo, M. I. Marqués, M. Laroche, J. J. Sáenz, Scattering forces from the curl of the spin angular momentum of a light field. *Phys. Rev. Lett.* **102**, 113602 (2009).
- D. B. Ruffner, D. G. Grier, Optical forces and torques in nonuniform beams of light. *Phys. Rev. Lett.* **108**, 173602 (2012).
- Y. Shen, X. Wang, Z. Xie, C. Min, X. Fu, Q. Liu, M. Gong, X. Yuan, Optical vortices 30 years on: OAM manipulation from topological charge to multiple singularities. *Light Sci. Appl.* **8**, 90 (2019).
- Z. Jin, D. Janoschka, J. Deng, L. Ge, P. Dreher, B. Frank, G. Hu, J. Ni, Y. Yang, J. Li, C. Yu, D. Lei, G. Li, S. Xiao, S. Mei, H. Giessen, F. M. zu Heringdorf, C.-W. Qiu, Phyllotaxis-inspired nanosieves with multiplexed orbital angular momentum. *eLight* **1**, 5 (2021).

60. Y. Shi, Y. Wu, L. K. Chin, Z. Li, J. Liu, M. K. Chen, S. Wang, Y. Zhang, P. Y. Liu, X. Zhou, H. Cai, W. Jin, Y. Yu, R. Yu, W. Huang, P. H. Yap, L. Xiao, W. Ser, T. T. B. Nguyen, Y.-T. Lin, P. C. Wu, J. Liao, F. Wang, C. T. Chan, Y. Kivshar, D. P. Tsai, A. Q. Liu, Multifunctional virus manipulation with large-scale arrays of all-dielectric resonant nanocavities. *Laser Photonics Rev.* **16**, 2100197 (2022).
61. G. Volpe, G. Volpe, Simulation of a Brownian particle in an optical trap. *Am. J. Phys.* **81**, 224–230 (2013).
62. V. Ginis, L. Liu, A. She, F. Capasso, Using the Belinfante momentum to retrieve the polarization state of light inside waveguides. *Sci. Rep.* **9**, 14879 (2019).
63. A. García-Etxarri, R. Gómez-Medina, L. S. Froufe-Pérez, C. López, L. Chantada, F. Scheffold, J. Aizpurua, M. Nieto-Vesperinas, J. J. Sáenz, Strong magnetic response of submicron silicon particles in the infrared. *Opt. Express* **19**, 4815–4826 (2011).
64. Y. Shi, H. Zhao, L. K. Chin, Y. Zhang, P. H. Yap, W. Ser, C.-W. Qiu, A. Q. Liu, Optical potential-well array for high-selectivity, massive trapping and sorting at nanoscale. *Nano Lett.* **20**, 5193–5200 (2020).
65. X. Chen, T. Li, H. Zeng, Z. Hu, B. Fu, Numerical and experimental investigation on micromixers with serpentine microchannels. *Int. J. Heat Mass Transfer* **98**, 131–140 (2016).
66. L. Liu, A. Woolf, W. Rodriguez Alejandro, F. Capasso, Absolute position total internal reflection microscopy with an optical tweezer. *Proc. Natl. Acad. Sci. U.S.A.* **111**, E5609–E5615 (2014).
67. Y. Shi, L.-M. Zhou, A. Q. Liu, M. Nieto-Vesperinas, T. Zhu, A. Hassanfiroozi, J. Liu, H. Zhang, D. P. Tsai, H. Li, W. Ding, W. Zhu, Y. F. Yu, A. Mazzulla, G. Cipparrone, P. C. Wu, C. T. Chan, C.-W. Qiu, Superhybrid mode-enhanced optical torques on Mie-resonant particles. *Nano Lett.* **22**, 1769–1777 (2022).

Acknowledgments

Funding: Y.S. was supported by the Fundamental Research Funds for the Central Universities. Y.S. and A.Q.L. acknowledge the Singapore Ministry of Education (MOE) Tier 3 grant (MOE2017-T3-1-001), Singapore National Research Foundation grant (MOH-000926), A*STAR

research grant (SERC A18A5b0056), and Singapore's National Water Agency grant (PUB-1804-0082). F.N. is supported, in part, by Nippon Telegraph and Telephone Corporation (NTT) Research, the Japan Society for the Promotion of Science (JSPS) [via the Grants-in-Aid for Scientific Research (KAKENHI), grant no. JP20H00134], the Army Research Office (ARO) (grant no. W911NF-18-1-0358), the Asian Office of Aerospace Research and Development (AOARD) (via grant no. FA2386-20-1-4069), and the Foundational Questions Institute Fund (FQXi) via grant no. FQXi-IAF19-06. D.P.T. acknowledges the support from the UGC/RGC of the HKSAR, China (project no. AoE/P-502/20 and GRF project 15303521); the Department of Science and Technology of Guangdong Province (no. 2020B1515120073); the Shenzhen Science and Technology Innovation Commission (grant no. SGDX2019081623281169); and the City University of Hong Kong (grant no. 9380131). T.Z. acknowledges the Natural Science Foundation of China (NSFC), grant no. 12104083. A.V.Z. acknowledges the support from the ERC iCOMM project (789340). P.C.W. acknowledges the support from the Ministry of Science and Technology (MOST), Taiwan (grant nos. 107-2923-M-006-004-MY3, 108-2112-M-006-021-MY3, and 110-2124-M-006-004), and, in part, from the Higher Education Sprout Project of the Ministry of Education (MOE) to the Headquarters of University Advancement at National Cheng Kung University (NCKU). P.C.W. also acknowledges the support from the Ministry of Education (Yushan Young Scholar Program), Taiwan. **Author contributions:** Y.S. conceived the idea. Y.S., T.Z., and P.C.W. performed the numerical simulations. Y.S., T.Z., D.P.T., J.L., H.Z., S.W., C.T.C., P.C.W., A.V.Z., F.N., and A.Q.L. were involved in the discussion and analysis. Y.S. and A.Q.L. conducted the experiment. Y.S., H.Z., S.W., C.T.C., A.V.Z., F.N., and A.Q.L. prepared the manuscript. Y.S., D.P.T., F.N., and A.Q.L. coordinated all the work. All authors commented on the manuscript. **Competing interests:** The authors declare that they have no competing interests. **Data and materials availability:** All data needed to evaluate the conclusions in the paper are present in the paper and/or the Supplementary Materials.

Submitted 12 November 2021

Accepted 17 October 2022

Published 30 November 2022

10.1126/sciadv.abn2291

Stable optical lateral forces from inhomogeneities of the spin angular momentum

Yuzhi Shi, Tongtong Zhu, Jingquan Liu, Din Ping Tsai, Hui Zhang, Shubo Wang, Che Ting Chan, Pin Chieh Wu, Anatoly V. Zayats, Franco Nori, and Ai Qun Liu

Sci. Adv., **8** (48), eabn2291.
DOI: 10.1126/sciadv.abn2291

View the article online

<https://www.science.org/doi/10.1126/sciadv.abn2291>

Permissions

<https://www.science.org/help/reprints-and-permissions>

Use of this article is subject to the [Terms of service](#)

Science Advances (ISSN) is published by the American Association for the Advancement of Science. 1200 New York Avenue NW, Washington, DC 20005. The title *Science Advances* is a registered trademark of AAAS.
Copyright © 2022 The Authors, some rights reserved; exclusive licensee American Association for the Advancement of Science. No claim to original U.S. Government Works. Distributed under a Creative Commons Attribution NonCommercial License 4.0 (CC BY-NC).